Vibrational analysis of thermal oscillations of single-walled carbon nanotubes under axial strain

Polina Pine,[1] Yuval E. Yaish,[2,*] and Joan Adler[3]

[1]*Russel Berrie Nanotechnology Institute, Technion, Haifa 32000, Israel*

[2]*Department of Electrical Engineering, Technion, Haifa 32000, Israel*

[3]*Department of Physics, Technion, Haifa 32000, Israel*

The first four flexural vibrational modes of single-walled carbon nanotubes (SWCNTs) of various lengths under different axial strains were studied using atomistic molecular dynamics within the framework of the Brenner interatomic potential and Fourier analysis. The simulated results are in excellent agreement with the Timoshenko beam model, which includes the effect of both rotary inertia and of shearing deformation. From the crossing points of the simulation data with the expected resonance frequencies of the unstrained tubes an upper limit for the effective SWCNT thickness is found ($\leqslant$0.1 nm), with no adjustable parameters. This partially resolves Yakobson's paradox concerning scattered estimates for nanotube width.

PACS number(s): 62.25.−g

I. INTRODUCTION

In the last few years intensive research on nano-electro-mechanical systems (NEMSs) based on carbon nanotubes (CNTs), has been made both experimentally and theoretically. Researchers measured the resonance frequencies of doubly clamped CNTs, studied dissipation processes within the vibrating tubes, and exploited their small mass to achieve ultralow mass sensitivities [1–11]. A key parameter in these experiments is the possibility of tuning the resonance frequencies by external gate electrodes. These gate electrodes, in addition to causing the tubes to vibrate at their resonance modes, also introduce an axial strain which modifies the resonance frequencies significantly [12,13]. Tuning is crucial for the implementation of such NEMS devices in future applications, such as filters, transducers, and sensors, and hence vibrational behavior under strain must be modeled.

There is a large body of simulation and analytic analysis modeling vibrational frequencies of CNTs. We have summarized the broad consensus that doubly clamped nanotubes have frequencies dependent on length and width but not on chirality in [14,15]. However, several studies show that there is a chirality dependence if the nanotubes are not doubly clamped [16–18]. Some aspects of these results are somewhat independent of the approach, be it direct simulation or an analytic model, but once the double clamping is relaxed (in imitation of the laboratory situation [16]), atomistic simulation is the most reliable way to characterize nanotube behavior.

In this paper we consider the effect of axial tension on the first four vibrational modes of single-walled carbon nanotube (SWCNT), using molecular dynamics (MD) and no fitting parameters. An early study of axial tension was made by [19] and more recent studies include those of [20,21]. These are limited to very small tensions (and compressions) and only the fundamental frequency has been deduced in most simulations. Analytic studies of tensioned tubes are complicated by possible variations in wall thickness under tension. An additional study of MD [13] and the analytic study of Sampaz *et al.* [12] introduce tension in their analysis, however, through

transversal electric fields which cause deformation of the tube in the direction perpendicular to its axis and stretching of the CNT. Moreover, the dynamic vibrations in Ref. [12] were significantly larger than the tube diameter and contributed as well to the beam elongation. In our study, the applied tensions are solely longitudinal, keeping the static vertical deformation of the tube at zero, and the axial symmetry of the tube is conserved. The vertical oscillations, which are driven by thermal noise, are less than the CNT diameter ($u < 0.1$ Å), hence, making their contribution to beam stretching negligible, and the tube motion is dominated by the interplay between the bending rigidity and the applied axial tension.

In a previous study [14] we introduced the Timoshenko beam model [22] to explain the simulation results for the vibrational modes of SWCNTs of different lengths and diameters. We gave a range of values for the product of the Young's modulus, E, and the nanotube width. We now extend this model to tensioned tubes and again obtain excellent agreement with the simulated results. The additional tension variable leads to cancellations at special "crossing points," which leads to an upper limit to the tube thickness with no free parameters. This bounds the widely varying estimates of this thickness known as Yakobson's paradox [23].

In the next section we present details of our simulations and results. In Sec. III we present analytical models and discuss their comparison with our numerical results. Conclusions are made in Sec. IV. In Appendix A we describe our full set of raw data and provide a comparison with an existing result for a stretched nanotube. In Appendix B we provide additional details of our Timoshenko beam model analysis.

II. SIMULATION DETAILS AND RESULTS

We validated our MD approach (Brenner interatomic potential [24] and predictor-corrector algorithm) in [14]; details and codes are given in [25]. Throughout the code development we generated still and animated atomic images with AViz [26] for verification purposes. An image of a (7,7) armchair nanotube of radius $R = 4.75$ Å and length $L = 98.38$ Å oriented along the y axis is shown in Fig. 1 [16]. Each ring of atoms is called a period [14]. We consider the four lowest vibrational modes, with wavelengths of $\lambda_n = 2L$, L, $2L/3$, and $L/2$,
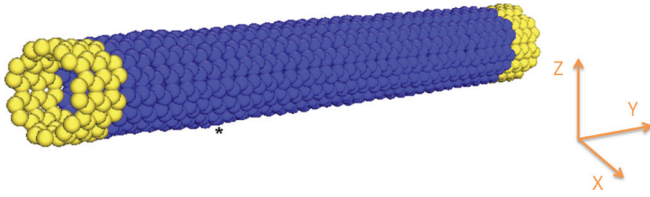
---

[*]yuvaly@ee.technion.ac.il

FIG. 1. (Color online) Doubly clamped (7,7) armchair nanotube. Three periods are frozen at each end [light gray (yellow online) atoms] and the remaining dark gray (blue online) atoms are free to move.

$n = 1$–4, respectively, and the effect of three different tensions, from initial lengths of $L = 98.38, 147.57, 196.76, 245.95$, and 295.14 Å; 20 tubes in total.

A Berendsen thermostat [27] was applied to maintain temperature. To ensure stable nanotube structure and eliminate intrinsic tension, we collected data after a period of slow initial thermalization to 300 K (periodic boundary conditions with no frozen edges), waiting until the length of the equilibrated nanotube remained constant up to insignificant fluctuations. The relaxed structures then had the three first periods clamped (frozen). Three stretched structures were prepared for each length as follows. The relaxed and equilibrated tubes had the last three free periods pulled in the positive y direction for elongation of an additional 2.5%, 5%, and 10% of the initial length. Then, the last three periods were also frozen to give doubly clamped boundary conditions. Initial calibration was conducted in order to delocalize intrinsic tension over the entire nanotube. To obtain adequate statistics we then let every nanotube vibrate 1000 times more than the period of its lowest frequency, using a MD time step of 0.5 fs. We then applied a fast Fourier transform (FFT) analysis to the data at several points [14,25], to calculate the power as a function of frequency for each nanotube. The frequencies are our primary means for comparing vibrations of different nanotubes. A full table of all the 80 vibrational modes is presented in Appendix A;
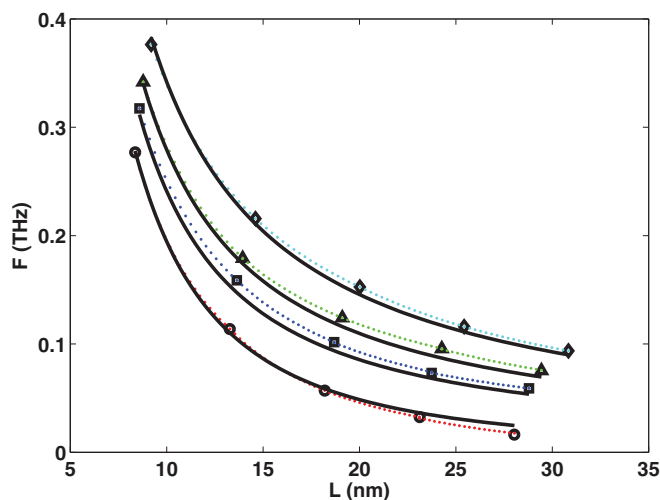

FIG. 2. (Color online) The fundamental mode as a function of length for $\epsilon = 0, 0.025, 0.5, 0.1$ (from bottom to top, respectively). Symbols are the simulated results, colored dotted lines are interpolated data, the continuous red line is best fit according to Eq. (2), and black lines are the solutions of EB beam equation [Eq. (1)].

the single set of published values [20] (of the lowest mode only) whose tension/width/length overlap ours fits in perfectly (see Fig. 11).

In Fig. 2 we plot the frequencies of the first mode for the unstrained and strained nanotubes ($\epsilon = 0, 0.025, 0.5$, and 0.1, in red, blue, green, and cyan, respectively, bottom to top) as a function of L. The graphs include raw data (with symbols larger than the error bars), interpolated (dotted) lines, and continuous fitted (red) and theoretical (black) lines. To enable comparison of frequencies for different tube tensions and modes, lengths should be the same. To achieve this we implement an interpolation procedure (dotted lines) [15] between adjacent points with the following length dependence: $f = \frac{a}{L} + \frac{b}{L^2}$ (see dashed lines in Fig. 2), where a and b are fitting parameters.

III. ANALYTICAL MODEL AND DISCUSSION

We now compare with theory for the case of residual tension, T_o, denoting angular frequency by ω, wall thicknesses [14] by h_m (mass wall thickness from graphite interlayer spacing) and h_e (wall thickness from elastic deformation), mass per unit length by m [2.27 fg for (7,7) tubes], and mass density by ρ. $A_{m(e)} = \pi(R + h_{m(e)}/2)^2 - (R - h_{m(e)}/2)^2$ are the tube cross sections. The moment of inertia is $I = \pi R h_e(4R^2 + h_e^2)/4$ and $m = \rho A_m$. The fundamental mode of the tube follows the expected Euler-Bernoulli (EB) beam equation [14] with parametrization of $p = L_0/L$, $L_0^2 = EI/T_0$, and $\beta^4 = \omega^2 m L^4/EI$,

$$\frac{\partial^4 u}{\partial \xi^4} - \frac{1}{p^2}\frac{\partial^2 u}{\partial \xi^2} = \beta^4 u, \tag{1}$$

where u is the transverse beam displacement (in either x or z direction) and $\xi = y/L$ is a dimensionless variable. Equation (1) has an analytical solution for the doubly clamped beam with any built in residual tension, and specifically for $T_0 = 0$, the solution for the first four modes yields values of $\beta_n^0 = 4.73, 7.85, 10.99, 14.13$, respectively [28], in the expression

$$f_n^0 = \frac{(\beta_n^0)^2}{2\pi}\sqrt{\frac{EI}{\rho A_m}}\frac{1}{L^2}. \tag{2}$$

As one can see from Eq. (2), these resonance frequencies depend on the bending rigidity EI, but not on E or I separately. Therefore, direct comparison with the simulated data cannot enable deduction of E and/or h_e. Nevertheless, for a given h_e the tube Young's modulus can be extracted. In Fig. 2 the continuous red line is the best fit to the data of the unstrained tube according to Eq. (2), with the bending rigidity (EI) as single fitting parameter. Assuming the generally accepted $h_e = 0.66$ nm, one receives $E = 3.04$ TPa, which is in good agreement with previous results [14]. Inserting this bending rigidity and solving Eq. (1) analytically for the vibrational modes of the strained tubes yields the other three continuous lines, drawn in black. As can be seen, the agreement between the simulation and theory is excellent, and it should be emphasized that for the three families of strained tubes, we did not use any fitting parameters.
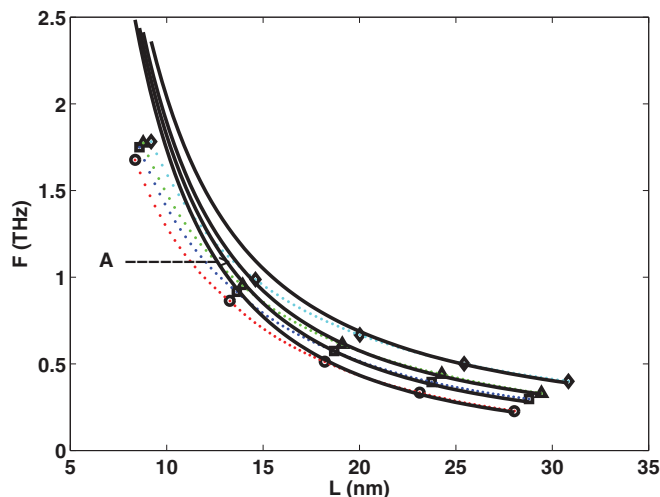
FIG. 3. (Color online) The fourth modes as functions of length for $\epsilon = 0, 0.025, 0.5, 0.1$ (bottom to top, respectively). Symbols are the simulated results, colored dotted lines are interpolated data, and continuous black lines are solutions of Eq. (1).

FIG. 4. (Color online) The second mode as a function of length for $\epsilon = 0, 0.025, 0.5, 0.1$ (from bottom to top, respectively). Symbols are the simulated results, colored dotted lines are interpolated data, and continuous black lines are the solutions of Eq. (1).

However, when we solve Eq. (1) for the higher vibrational modes (with and without strain) and compare the results with the simulated data, we found no satisfactory agreement at all. For example, in Fig. 3 we show the simulated results (colored dots) of the fourth mode as a function of tube length for the different strains. The continuous black lines [solution of Eq. (1) according to the EB model] are in good agreement at large L, but as L decreases the deviation between simulation and model increases. This behavior was observed in [14] for the unstrained tube and attributed to softening of the tube tension (compression) according to the Timoshenko beam model [29]. This model takes into account shear deformation and rotational inertia effects, which become significantly for short beams and high resonance modes. The crossover occurs when $\mu = R/\lambda_n > 0.05$. Similar graphs for the second and third modes are shown in Figs. 4 and 5, respectively.

The Timoshenko beam model has the same form as Eq. (1) but with the following expressions for the parameters:

$$\frac{1}{p^2} = \frac{A_e E \epsilon L^2}{EI} - \frac{\omega^2 m L^2}{A_m E} \left(1 + \frac{A_m E}{A_e G k} \right), \quad (3)$$

$$\beta^4 = \frac{\omega^2 m L^4}{EI} \left(1 - \frac{\omega^2 m I}{A_m A_e G k} \right), \quad (4)$$

where G is the shear modulus and k is the Timoshenko shear coefficient, which depends on the geometry. Normally, $k = 9/10$ for circular cross sections. The first term in Eq. (3) arises from the positive residual tension, $T_0 > 0$, whereas the second term is responsible for the shear deformation. These two terms have opposite signs, and as a result the first term increases the vibrational modes (elongation), but the second makes the beam softer (compression). The role of the second term becomes more significant as the frequencies increase, in agreement with the simulated results (Figs. 3, 4, and 5). For example, let us observe point A in Fig. 3. For larger L values, the vibrational modes of the studied SWCNTs under
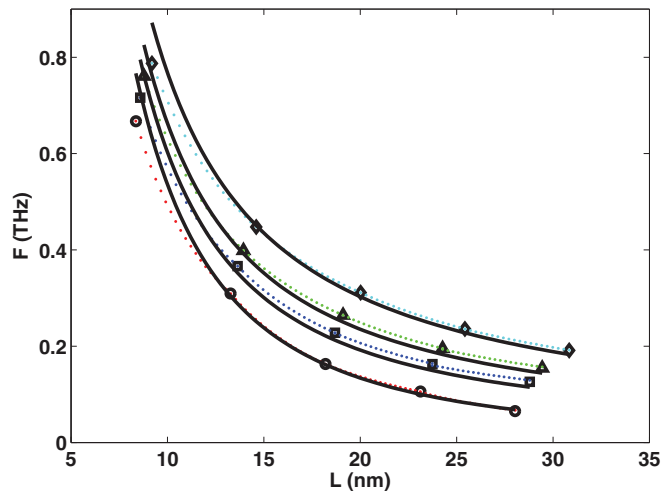
residual strain of $\epsilon = 0.05$ (green dotted line) are higher than the vibrational frequencies of the unstrained tubes (black line). However, to the left of this point (shorter lengths) the negative contribution to the residual tension becomes dominant and the tubes are under compression, which results in lower resonance frequencies with respect to the zero strain case ($\epsilon = 0$).

There are special frequencies, f_0 (similar to point A), at which these two terms cancel each other, and the tube is under no tension at all. Since the contribution of the second term in Eq. (4) is small at these frequencies as explained in Appendix B, the expected resonance modes should follow the solution of the EB beam model under zero strain, f_n^0. The f_0 are crossing points between the continuous lines and the simulated data (see Figs. 3, 4, and 5), and obey the following
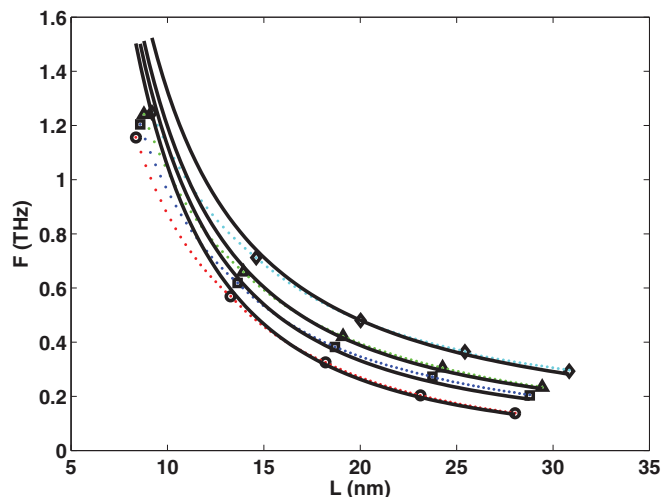

FIG. 5. (Color online) The third mode as a function of length for $\epsilon = 0, 0.025, 0.5, 0.1$ (from bottom to top, respectively). Symbols are the simulated results, colored dotted lines are interpolated data, and continuous black lines are the solutions of Eq. (1).
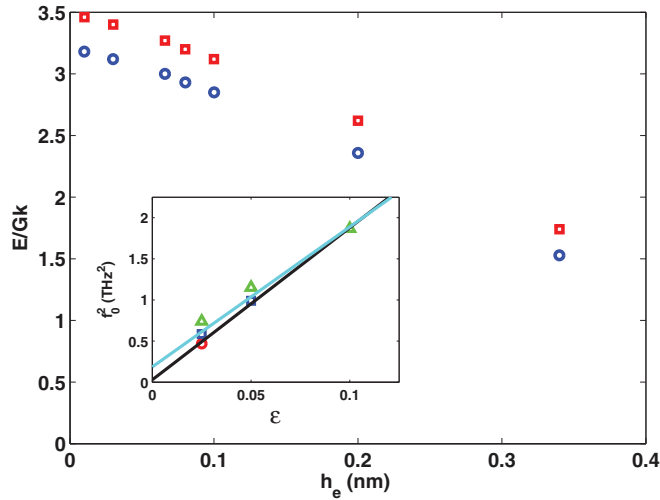
FIG. 6. (Color online) E/Gk vs tube thickness, h_e. Red squares (blue circles) were extracted from the crossing frequencies analysis of the complete (highest) data set, as discussed in the main text. (Inset) f_0^2 vs ϵ for a given $h_e = 0.066$ nm. Green triangles, blue rectangles, and the red circle are the crossing frequencies of the fourth, the third, and the second modes with the frequencies of the same modes for the unstrained tubes, respectively. Cyan (black) lines are the best fits to linear behavior of the complete (highest) crossing frequencies analysis.

relation:

$$f_0^2 = \frac{1}{(2\pi)^2} \frac{A_e A_m E}{Im} \left(1 + \frac{A_m}{A_e} \frac{E}{Gk} \right)^{-1} \epsilon. \qquad (5)$$

The inset of Fig. 6 depicts f_0^2 vs ϵ as extracted from Figs. 3, 4, and 5. The two lines are best fits to the linear relation of all the crossing points (cyan) and to the highest of each mode, $f_0^{\max}$ (black). In Appendix B we explain why the approximation we have used is more justified for $f_0^{\max}$, as is evident from the superior linear fitting that cross the origin for zero strain. From the slope of these lines one can extract E/Gk and compare to the theoretical value of $E/Gk = 2(1 + \nu)/k = 3 \pm 0.1$, where $\nu = 0.3$–0.4 is the Poisson ratio of SWCNTs [19,30]. This value of E/Gk is consistent with previous result that we have discussed in Ref. [14].

In the current analysis we have used $h_e = 0.066$ nm. As mentioned before, the EB beam model depends only on the bending rigidity, EI, and not on each of them separately. We could repeat the previous analysis with other values of h_e, and study if and how E/GK is modified. The results of such analysis are depicted in Fig. 6 where E/Gk is plotted vs h_e. Red circles originate from the whole data set (cyan line in Fig. 6, inset), and blue circles are due to the highest data points from each mode (black line in Fig. 6). Surprisingly, for $h_e \leqslant 0.1$ nm E/Gk tends to saturate at the theoretical value of ≈ 3, but for higher values of h_e, there is a substantial drop in the values of E/Gk, suggesting that these values for the elastic tube thickness are erroneous, thus placing an upper limit on Yakobson's paradox. This result is in good agreement with Ref. [14], based on diameter analysis of the vibrational modes, as well as, [18], who based their results on a continuum model.
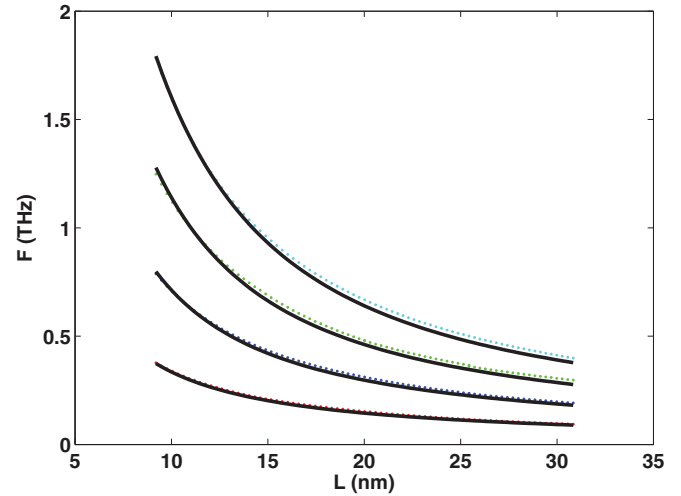

FIG. 7. (Color online) The first four vibrational modes as a function of length for $\epsilon = 0.1$ (from bottom to top, respectively). Red, blue, green, and cyan are the interpolated simulated results, and continuous black lines are the solutions of Eqs. (1), (3), and (4) without any fitting parameter.

Given the values of the bending rigidity from the Young's modulus ($E = 3.04$ TPa), the tube thickness ($h_e = 0.66$ nm), and $E/Gk = 3$, there are no fitting parameters left in Eqs. (1), (3), and (4). Hence, one can solve this set of equations (frequencies vs lengths) and compare them to the simulated results. The procedure to solve these equations is the following. Equation (1) has an analytical solution for any value of residual tension, T_0. However, the expression is quite cumbersome for $T_0 \neq 0$, but may be defined in the following relation: $\beta_n = \mathcal{F}(T_0 L^2/EI) = \mathcal{F}(1/p^2)$. From the definition of β_n one may extract the expected resonance frequencies. Inserting these frequencies back into Eqs. (3) and (4) and solving them self-consistently yields the resonance modes vs tube lengths

FIG. 8. (Color online) The first four vibrational modes as a function of length for $\epsilon = 0$ (from bottom to top, respectively). Red, blue, green, and cyan are the interpolated simulated results, and continuous black lines are the solutions of Eqs. (1), (3), and (4) without any fitting parameter.
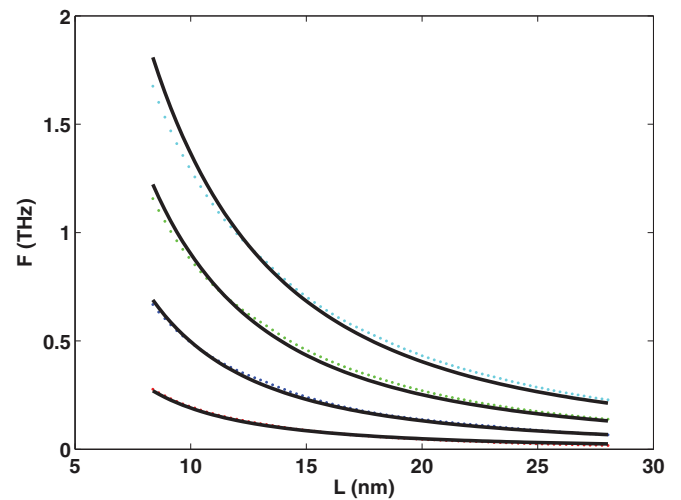
FIG. 9. (Color online) The first four vibrational modes as a function of length for $\epsilon = 0.025$ (from bottom to top, respectively). Red, blue, green, and cyan are the interpolated simulated results, and continuous black lines are the solutions of Eqs. (1), (3), and (4) without any fitting parameter.
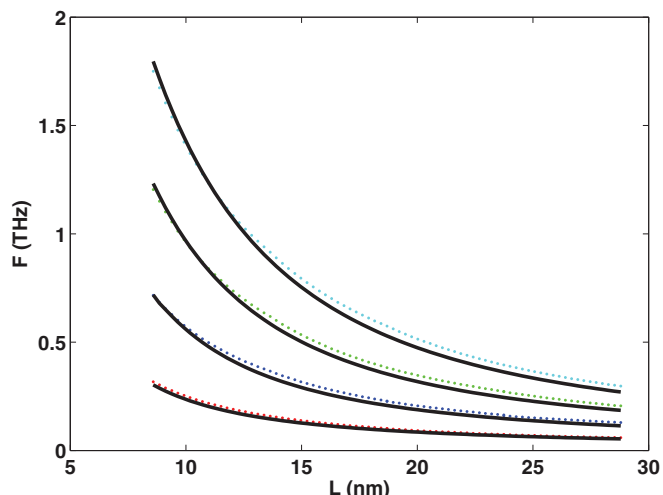
for any given strain. The results of this analysis are plotted in Figs. 7–10. As evident from this graph, the agreement between the simulated data and the theoretical model is excellent. We emphasize that there is no fitting parameter in these figures.

IV. CONCLUSIONS

In summary, we presented a detailed atomistic MD simulation and analysis of the thermal vibrational modes of SWCNTs subjected to axial strain within the Brenner interatomic potential. The simulation spans substantial range of tube length and strain (up to 10%) and agrees well with EB continuum beam model for the fundamental mode. However, for higher modes and bigger $\mu = R/\lambda$ ratios the data deviate significantly
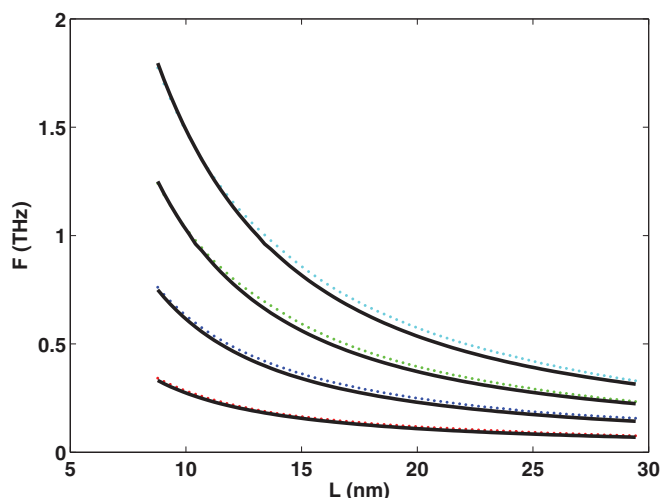

FIG. 10. (Color online) The first four vibrational modes as a function of length for $\epsilon = 0.05$ (from bottom to top, respectively). Red, blue, green, and cyan are the interpolated simulated results, and continuous black lines are the solutions of Eqs. (1), (3), and (4) without any fitting parameter.

from the predicted model, and an alternative model (known as the Timoshenko beam model) that takes into account the effects of rotary inertia and shearing deformation was adopted. From comparison between the simulated data and the EB beam model for the unstrained tube, we could extract the value of $E/Gk \approx 3$, in agreement with the continuum model, and obtain an upper limit for the tube elastic thickness, $h_e \leqslant 0.1$ nm, thus partially resolving Yakobson's paradox. This paradox originates from the fact that in most of the mechanical equations the bending rigidity, I, and the Young's modulus, E, appear together; thus, it is not a simple task to measure them separately. This challenge is very relevant to CNTs, since the thickness which is attributed to the mechanical strain is unclear. The main point is that the distance between the graphene layers is not obviously the thickness that is relevant for mechanical experiments. In this paper we show that in our simulation and theoretical analysis above a critical thickness the ratio between the Young's modulus and the shear modulus changes, and, hence, an upper limit for the tube mechanical thickness is suggested. This conclusion agrees with our previous result, which was derived from completely different arguments. We believe that these two independent results, which support each other, will assist future analysis of experimental results of mechanical experiments in CNTs. Finally, comparison between the simulated data and the anticipated resonance modes according to the Timoshenko beam model gives excellent agreement for all four modes without any fitting parameter.

APPENDIX A: RAW DATA AND COMPARISON

We present the full set of frequencies below. We also compare our fundamental mode frequencies as a function of length with the only other results of this type we could find. Our initial relaxed (7,7) SWCNTs had lengths (L) of 98.38, 147.57, 196.76, 245.95, and 295.14 Å, all with a diameter, D (= $2R$) of 9.5 Å. Due to the fact that three last/first periods are frozen the relaxed vibrating fragments of the nanotubes are 83.62, 132.81, 182.00, 231.19, and 280.38 Å long, respectively. The lengths of the nanotubes after applied tension are presented in Table I. For later reference we also include values of a parameter L/D in this table. It is used by other authors to characterize nanotubes and index the vibrations of the fundamental mode. In our previous studies we used a parameter we call $\mu = R/\lambda$, as introduced in Ref. [14], which indexes all modes of vibration. For the fundamental mode these are exact inverses, but μ is a function of mode as well as nanotube geometry, and is needed in order to exploit the extra information provided by the four modes. The large μ values characteristic of higher modes describe the region where only the Timoshenko beam model [22] fits the data and the simpler EB model fails. We return to this in our discussion below.

TABLE I. Data sets of first four vibrational modes (in Hz) and vibrating lengths of relaxed and 2.5%, 5%, and 10% stretched armchair (7,7) nanotubes. Dimensionless L/D values for the untensioned tube (of both the vibrating part and the entire tube) are also given.

Vibrating L/D	8.80	13.98	19.16	24.34	29.51
Complete L/D	10.36	15.53	20.71	25.89	31.07
L_v^0 (Å)	83.62	132.81	182.00	231.19	280.38
f_1	2.77×10^{11}	1.14×10^{11}	5.70×10^{10}	3.26×10^{10}	1.63×10^{10}
f_2	6.67×10^{11}	3.09×10^{11}	1.63×10^{11}	1.06×10^{11}	6.51×10^{10}
f_3	1.16×10^{12}	5.697×10^{11}	3.26×10^{11}	2.04×10^{11}	1.38×10^{11}
f_4	1.68×10^{12}	8.62×10^{11}	5.13×10^{11}	3.34×10^{11}	2.28×10^{11}
$L_v^{2.5\%}$ (Å)	85.71	136.13	186.55	236.97	287.39
f_1	3.17×10^{11}	1.59×10^{11}	1.02×10^{11}	7.32×10^{10}	5.90×10^{10}
f_2	7.16×10^{11}	3.66×10^{11}	2.28×10^{11}	1.63×10^{11}	1.26×10^{11}
f_3	1.20×10^{12}	6.19×10^{11}	3.83×10^{11}	2.73×10^{11}	2.04×10^{11}
f_4	1.75×10^{12}	9.16×10^{11}	5.74×10^{11}	3.95×10^{11}	2.97×10^{11}
$L_v^{5\%}$ (Å)	87.80	139.45	191.10	242.75	294.40
f_1	3.42×10^{11}	1.79×10^{11}	1.24×10^{11}	9.56×10^{10}	7.53×10^{10}
f_2	7.61×10^{11}	4.00×10^{11}	2.65×10^{11}	1.95×10^{11}	1.55×10^{11}
f_3	1.24×10^{12}	6.59×10^{11}	4.21×10^{11}	3.05×10^{11}	2.34×10^{11}
f_4	1.77×10^{12}	9.52×10^{11}	6.12×10^{11}	4.40×10^{11}	3.30×10^{11}
$L_v^{10\%}$ (Å)	91.98	146.09	200.20	254.31	308.42
f_1	3.76×10^{11}	2.16×10^{11}	1.53×10^{11}	1.16×10^{11}	9.36×10^{10}
f_2	7.87×10^{11}	4.48×10^{11}	3.11×10^{11}	2.36×10^{11}	1.91×10^{11}
f_3	1.25×10^{12}	7.12×10^{11}	4.80×10^{11}	3.64×10^{11}	2.93×10^{11}
f_4	1.78×10^{12}	9.87×10^{11}	6.67×10^{11}	5.01×10^{11}	3.99×10^{11}

Our raw data are summarized in Table I. Lengths are quoted with two significant figures after the decimal point and errors on the frequencies are limits of reading, of $\pm 0.005 \times 10^{11}$ Hz. In Fig. 11 we show frequency as a function of strain for the fundamental mode for our five different lengths. The data from
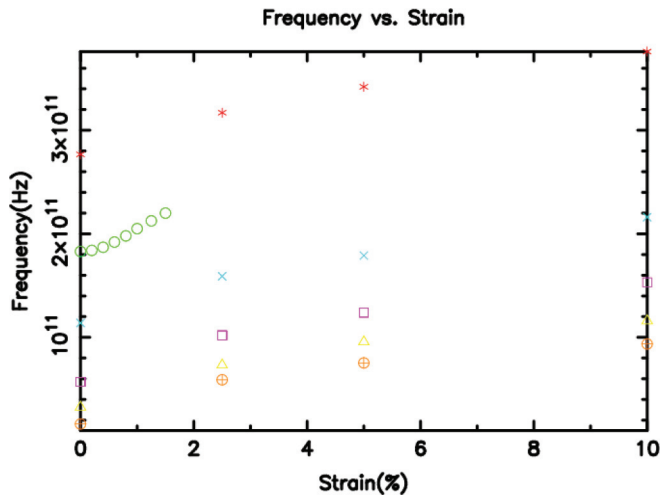

FIG. 11. (Color online) Fundamental mode frequency in Hz as a function of axial tension from our results and from Zhang et al. [20]. The uppermost curve (dark ∗, red online) is for our smallest $L/D = 10.36$ and the next curve down (○, green online) is from Zhang et al. with $L/D = 13$. The following curves are for our successively increasing lengths [$L/D = 15.53$, × (turquoise online); $L/D = 20.71$, □ (magenta online); $L/D = 25.89$, △ (yellow online); $L/D = 31.07$, ⊕ (orange online)] with the longest at the bottom of the graph.

the tube with the smallest L/D value appears at the top of the graph. We also include the data from Zhang et al. [20] (read off their graph). If we estimate L/D for our tubes using the full length (including the six clamped periods), it fits nicely into our sequence. We note that there is a discussion of fits to an analytic model presented by Zhang et al. [20] that uses the nanotube width as a free parameter, and they in fact provide different fits for different width choices. We have shown [14] that one needs to consider frequencies of higher modes as well for a reliable analysis. The discussion presented by Zhang et al. based on the shell model [21] also does not consider higher modes under strain.

APPENDIX B: DETAILS OF TIMOSHENKO BEAM MODEL ANALYSIS

In the main text, we based our analysis of f_0^2 vs ϵ on the cancellation of $1/p^2$ term of Eq. (3). To be more precise, the crossing frequencies, f_0, between the interpolated simulated results and the unstrained EB vibrational modes should satisfy the equations (substituting full expressions for some parameters)

$$\frac{1}{p^2} \frac{\partial^2 u}{\partial \xi^2} = \frac{\omega_0^2 m L^4}{EI} \left(\frac{\omega_0^2 m I}{A_m A_e G k} \right) u, \tag{B1}$$

$$\frac{A_e E \epsilon L^2}{EI} - \frac{\omega_0^2 m L^2}{A_m E} \left(1 + \frac{A_m E}{A_e G k} \right) \frac{\partial^2 u}{\partial \xi^2}$$

$$= \frac{\omega_0^2 m L^4}{EI} \left(\frac{\omega_0^2 m I}{A_m A_e G k} \right) u, \tag{B2}$$

where $\omega_0 = 2\pi f_0$. At the crossing points, the transverse beam displacement, $u(\xi)$, has an analytical expression; thus, one can multiply Eq. (B2) by u or by its even derivatives, and integrate

over the entire beam length. The result of this analysis enables one to obtain a more accurate estimation for E/Gk. It turns out regardless of which function (u or its even derivatives) one multiplies and integrates, the general outcomes is

$$E/Gk = (E/Gk)_0 \frac{1}{1+a}, \qquad \text{(B3)}$$

where $(E/Gk)_0$ is the result obtained from the requirement that $1/p^2 = 0$, and $a \ll 1$. a contains ratios of derivatives, where the denominator always consists of two additional space derivatives with respect to the numerator. As a result, $a \ll 1$, and our approximation is better justified for the highest crossing frequencies of each mode, $f_0^{\max}$.

[1] V. Sazonova, Y. Yaish, H. Ustunel, D. Roundy, T. A. Arias, and P. L. McEuen, Nature (London) **431**, 284 (2004).

[2] A. K. Huttel, G. A. Steele, B. Witkamp, M. Poot, L. P. Kouwenhoven, and H. S. J. van der Zant, Nano Lett. **9**, 2547 (2009).

[3] B. Lassagne, Y. Tarakanov, J. Kinaret, D. Garcia-Sanchez, and A. Bachtold, Science **325**, 1107 (2009).

[4] G. A. Steele, A. K. Huttel, B. Witkamp, M. Poot, H. B. Meerwaldt, L. P. Kouwenhoven, and H. S. J. van der Zant, Science **325**, 1103 (2009).

[5] A. Eichler, J. Moser, J. Chaste, M. Zdrojek, I. Wilson-Rae, and A. Bachtold, Nat. Nanotechnol. **6**, 339 (2011).

[6] H.-Y. Chiu, P. Hung, H. W. C. Postma, and M. Bockrath, Nano Lett. **8**, 4342 (2008).

[7] B. Lassagne, D. Garcia-Sanchez, A. Aguasca, and A. Bachtold, Nano Lett. **8**, 3735 (2008).

[8] J. Chaste, A. Eichler, J. Moser, G. Ceballos, R. Rurali, and A. Bachtold, Nat. Nanotechnol. **7**, 301 (2012).

[9] A. Castellanos-Gomez, H. B. Meerwaldt, W. J. Venstra, H. S. J. van der Zant, and G. A. Steele, Phys. Rev. B **86**, 041402(R) (2012).

[10] E. Laird, F. Pei, W. Tang, G. Steele, and L. Kouwenhoven, Nano Lett. **12**, 193 (2012).

[11] J. Island, V. Tayari, A. McRae, and A. Champagne, Nano Lett. **12**, 4564 (2012).

[12] S. Sapmaz, Y. M. Blanter, L. Gurevich, and H. S. J. van der Zant, Phys. Rev. B **67**, 235414 (2003).

[13] C. Y. Wang and L. C. Zhang, Nanothechnology **19**, 195704 (2008).

[14] P. Pine, Y. E. Yaish, and J. Adler, Phys. Rev. B **83**, 155410 (2011).

[15] P. Pine, Y. E. Yaish, and J. Adler, Phys. Rev. B **84**, 245409 (2011).

[16] P. Pine, Y. E. Yaish, and J. Adler, J. Appl. Phys. **110**, 124311 (2011).

[17] S. S. Gupta, F. G. Bosco, and R. C. Batra, J. Appl. Phys. **106**, 063527 (2009).

[18] Y. Huang, J. Wu, and K. C. Hwang, Phys. Rev. B **74**, 245413 (2006).

[19] G. Cao, X. Chen, and J. W. Kysar, Phys. Rev. B **72**, 235404 (2005).

[20] Y. Y. Zhang, C. M. Wang, and V. B. C. Tan, Adv. Appl. Math. Mech. **1**, 89 (2009).

[21] B. Arash and R. Ansari, Physica E **42**, 2058 (2010).

[22] S. P. Timoshenko and J. N. Goodier, *Theory of Elasticity*, 3rd ed. (McGraw Hill, New York, 1987).

[23] B. I. Yakobson, C. J. Brabec, and J. Bernholc, Phys. Rev. Lett. **76**, 2511 (1996).

[24] D. W. Brenner, Phys. Rev. B **42**, 9458 (1990).

[25] P. Pine, Ph.D. thesis, Technion, 2012, http://phycomp.technion.ac.il/~newphr76ja/polina.pdf.

[26] http://phycomp.technion.ac.il/~aviz.

[27] H. Berendsen, J. Postma, W. van Gunsteren, A. DiNola, and J. Haak, J. Chem. Phys. **81**, 3684 (1984).

[28] L. D. Landau and E. M. Lifshitz, *Elasticity Theory* (Pergamon, Oxford, UK, 1986).

[29] S. P. Timoshenko, D. H. Young, and J. W. Weaver, *Vibration Problems in Engineering*, 4th ed. (Wiley & Sons, New York, 1974).

[30] J. P. Lu, Phys. Rev. Lett. **79**, 1297 (1997).